Available online at www.sciencedirect.com
SCIENCE DIRECT
Physica E 31 (2006) 142–147
PHYSICA E
www.elsevier.com/locate/physe

Anisotropic magnetoresistance and spin-valve effect in all-metal mesoscopic spin-valve devices

Alexander van Staa*, Guido Meier

Institut für Angewandte Physik und Zentrum für Mikrostrukturforschung, Universität Hamburg, Jungiusstrasse 11, 20355 Hamburg, Germany

Received 24 October 2005; accepted 1 November 2005
Available online 28 February 2006

Abstract

We have fabricated all-metal lateral spin-valve devices consisting of two permalloy electrodes and an interconnecting aluminum strip. The micromagnetic behavior of the device has been imaged with a magnetic-force microscope in external magnetic fields at room temperature. During a single cooling cycle at temperatures between 2 and 120 K we have measured the anisotropic magnetoresistance of both electrodes and the magnetoresistance of the entire device. In the latter, we can clearly identify the contributions of the anisotropic magnetoresistance and the mesoscopic spin-valve effect.

PACS: 72.25.Ba; 73.23.−b

Keywords: Spin-polarized transport; Magnetoresistance; Spin-valve effect

1. Introduction

The quest for all-electrical spin detection in mesoscopic hybrid devices is still in its infancy. Only in a very limited number of experiments, electrical spin injection, either into semiconductors [1,2] or into normal metals [3], has been achieved. The ongoing interest in spintronic devices is fuelled by the predicted velocity of operation and the enhanced functionality given by the spin as a further degree of freedom. Those features might add to devices which use magnetoresistance effects like the giant magnetoresistance [4], the tunnelling magnetoresistance [5,6] and the anisotropic magnetoresistance [7–9]. All these magnetoresistance effects are connected to the electron spin and are already used in hard disk read heads, magnetic random access memories or magnetic field sensors. In this work we focus on lateral ferromagnet/normal metal spin-valve devices.

A current flowing from a ferromagnet (F) into a normal metal (N) creates a spin polarization in the normal metal. Because of different conductivities of spin-up and spin-down electrons in the ferromagnet, the chemical potentials of both kinds of charge carriers are split up at the interface. Therefore, the spin polarization of a ferromagnet can be partly transferred into a normal metal within the spin-relaxation length λ_N of the normal metal [10]. With a F/N/F structure both electrical spin injection and detection can be realized in a single device if the length of the normal metal is in the range of λ_N. We use a lateral mesoscopic spin-valve device consisting of two bar-shaped parallel permalloy ($Ni_{80}Fe_{20}$) electrodes with a strong shape anisotropy and an interconnecting aluminum strip (see Fig. 1). Due to the shape anisotropy each electrode virtually consists of a single magnetic domain which is aligned along the long axis of the electrode. The antiparallel configuration of their magnetizations leads to an increased resistance in comparison to the parallel configuration.

After a theoretical description of a F/N/F structure in Section 2 we report in Section 3 on the sample preparation and the micromagnetic properties of the ferromagnetic electrodes. The anisotropic magnetoresistances of both electrodes and the magnetoresistance of the entire device

*Corresponding author. Tel.: +49 40 42838 5784; fax: +49 40 42838 3954.
E-mail address: astaa@physnet.uni-hamburg.de (A. van Staa).

1386-9477/$ - see front matter © 2006 Elsevier B.V. All rights reserved.
doi:10.1016/j.physe.2005.11.006

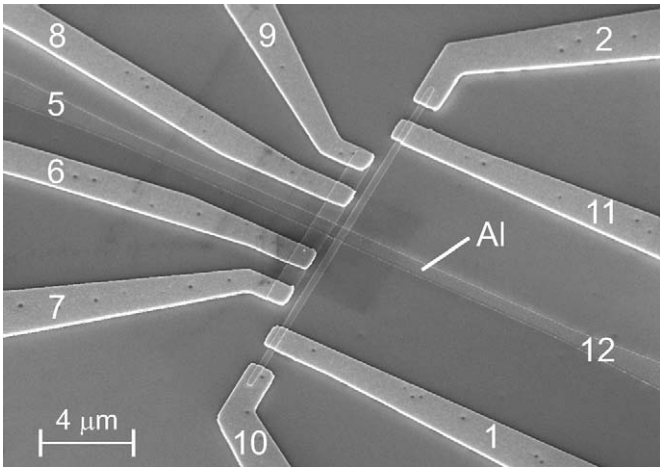

Fig. 1. Scanning-electron micrograph of the F/N/F device. The aluminum strip is labelled 5 and 12 on its left and right sides, respectively. The leads with the numbers 6–9 are gold contacts to the shorter permalloy electrode. The gold leads to the longer permalloy electrode are numbered 1, 2, 10 and 11.

are measured during a single cooling cycle. This enables us to identify the contributions of the anisotropic magnetoresistance and the spin-valve effect to the overall magnetoresistance which will be discussed in Section 4.

2. Theoretical description

We follow the theoretical approach by van Son et al. [10] who have described the boundary resistance of a single ferromagnet/normal metal interface. Assuming that the spin-relaxation length of the electrons is much longer than their mean free path, the electron transport can be described in a two-current model in which the spin-up and spin-down electrons behave independently. Therefore, one can define different current densities $j_{\uparrow,\downarrow}$ and conductivities $\sigma_{\uparrow,\downarrow} = (1 \pm \alpha)\sigma/2$ where α and σ are the bulk current spin-polarization and the spin-independent conductivity of the materials (α_F, σ_F for the ferromagnet and $\alpha_N = 0, \sigma_N$ for the normal metal). Using Ohm's law the gradients of the chemical potentials of the spin-up and spin-down electrons are

$$\partial\mu_{\uparrow,\downarrow}/\partial x = -(e/\sigma_{\uparrow,\downarrow})j_{\uparrow,\downarrow}. \quad (1)$$

In the steady state, the difference in the chemical potentials obeys the diffusion equation

$$(\mu_\uparrow - \mu_\downarrow)/\tau_{F,N} = D_{F,N}\partial^2(\mu_\uparrow - \mu_\downarrow)/\partial x^2, \quad (2)$$

with the diffusion constant $D_{F,N} = \frac{1}{3}v_{F,N}l_{F,N}$, the spin-relaxation rate $\tau_{F,N}^{-1}$, the Fermi velocity $v_{F,N}$ and the mean free path of the electron $l_{F,N}$ (index F in the ferromagnet and index N in the normal metal). The spin-relaxation length is defined as $\lambda_{F,N} = \sqrt{D_{F,N}\tau_{F,N}}$. In a system with two ferromagnets which are semi-infinite in x-direction and a normal metal of length L between them, the chemical potentials $\mu_\uparrow$ and $\mu_\downarrow$ in each part of the device can be obtained by solving the diffusion equation. The continuity of both chemical potentials and current densities have to be regarded as boundary conditions. The chemical potentials for a typical set of parameters ($\alpha_F = 0.37$, $\sigma_F = 3.7 \times 10^6\,\Omega^{-1}\,m^{-1}$, $\sigma_N = 8.6 \times 10^6\,\Omega^{-1}\,m^{-1}$, $\lambda_F = 5\,nm$, $\lambda_N = 120\,nm$, $L = 350\,nm$ and a current density j of $50\,\mu A/(25\,nm \times 600\,nm)$) are depicted in Fig. 2(b) and (c) for the parallel and the antiparallel configurations of the magnetizations of the ferromagnets, respectively. For direct comparison with the experimental values the chemical potentials are converted to voltages. The dominant linear parts of $\mu_\uparrow$ and $\mu_\downarrow$ generated by the spin-independent conductivities σ_F and σ_N are subtracted for clarity, i.e., to make the spin-related effects visible. The voltage drop over the normal metal alone is 135 μV in the example of Fig. 2 and therefore two orders of magnitude larger than the splitting of the chemical potentials. The average chemical potential which can be measured with

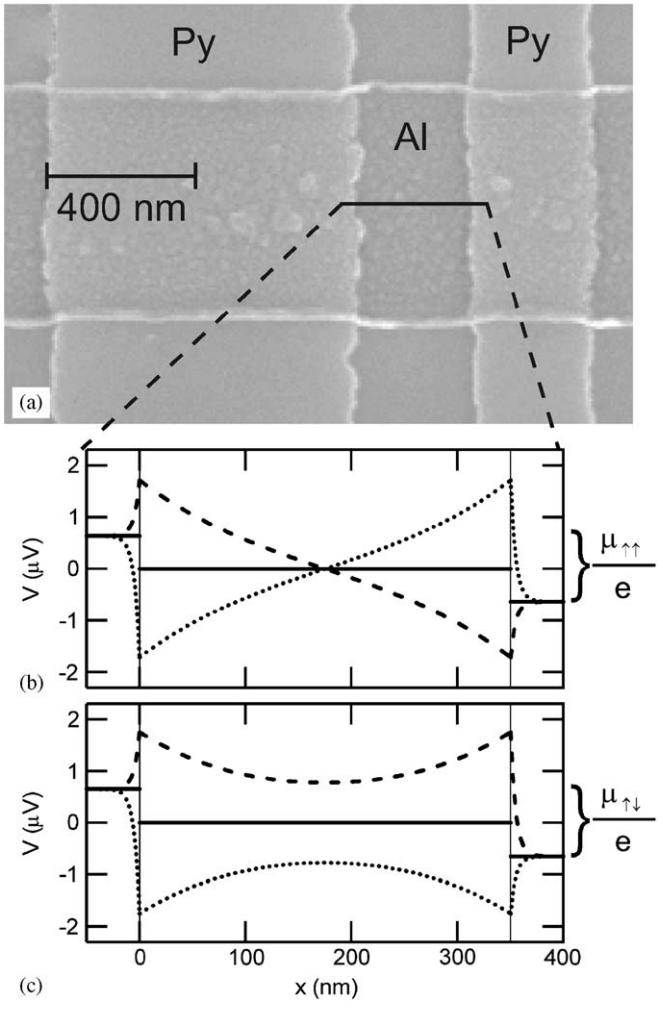

Fig. 2. (a) Scanning-electron micrograph of the crossing region of the two permalloy electrodes and the aluminum strip. In (b) and (c) the spatial dependences of the chemical potentials, converted to voltages, of the spin-up (dashed line) and spin-down (dotted line) electrons are depicted for the parallel and the antiparallel configurations of the magnetizations of the electrodes, respectively. The F/N interfaces are at $x = 0$ and 350 nm. The solid lines denote the resulting average chemical potentials.

voltage probes is defined as $\mu_0 = (1+\alpha)/2 * \mu_\uparrow + (1-\alpha)/2 * \mu_\downarrow$ and is shown in Fig. 2(b) and (c) as solid lines. The discontinuity at the interfaces causes the spin-dependent boundary resistances. The voltage drops between the two ferromagnets are $\mu_{\uparrow\uparrow}/e$ and $\mu_{\uparrow\downarrow}/e$ for the parallel and the antiparallel configuration of the magnetizations, respectively. From the solution of the diffusion equation we derive the difference

$$\Delta\mu = \mu_{\uparrow\downarrow} - \mu_{\uparrow\uparrow} = \frac{4e\alpha_F^2(1-\alpha_F^2)^{-1}\lambda_F\sigma_F^{-1}}{2\cosh(L/\lambda_N) + [C + C^{-1}]\sinh(L/\lambda_N)} j \quad (3)$$

with the constant

$$C = (1-\alpha_F^2)\frac{\sigma_F\lambda_N}{\sigma_N\lambda_F}. \quad (4)$$

This means a change in resistance $\Delta R = \Delta\mu/eI$ of the entire device when the relative orientation of the magnetizations is altered. For the exemplary set of parameters used for Fig. 2 the voltage $\Delta\mu/e$ is 28 nV underlining the challenge to measure it.

3. Sample preparation and micromagnetic behavior

The spin-valve devices are fabricated with three different successively employed electron-beam lithography resist masks. At first, the two permalloy electrodes are thermally evaporated on a semi-insulating GaAs(1 0 0) substrate. The shorter electrode measures 8 μm × 800 nm, the longer electrode 16 μm × 300 nm. Both electrodes have a thickness of 30 nm and the spacing between the electrodes is $L = 350$ nm. It is essential to start with the permalloy electrodes on the flat substrate to ensure a reliable and simple micromagnetic behavior. Permalloy electrodes deposited on top of an aluminum strip show a complicated domain configuration [11]. With the second resist mask the aluminum strip is deposited on top of the electrodes via DC magnetron sputtering. Before the deposition an in situ argon RF-plasma etching step is performed to remove naturally grown oxides on top of the electrodes and thus to obtain clean interfaces between permalloy and aluminum. The aluminum strip has a width of 600 nm and a thickness of 25 nm. Finally, the permalloy electrodes are contacted via thermally evaporated gold leads as depicted in Fig. 1.

The stray fields of the electrodes have been recorded with a magnetic-force microscope at room temperature in an external magnetic field. In Fig. 3, one can clearly see that each electrode consists of a quasi-single domain as a result of the strong shape anisotropy [12]. With the external magnetic field applied parallel to the long axes of the electrodes the magnetizations can be set to a parallel configuration (Fig. 3(b) and (d)) or an antiparallel configuration (Fig. 3(c) and (e)) as indicated by the arrows. The coercive fields of the shorter and the longer electrode are ±5.5 and ±21 mT, respectively. Significantly different switching fields of the electrodes are important to detect resistance effects in spin-valve devices.

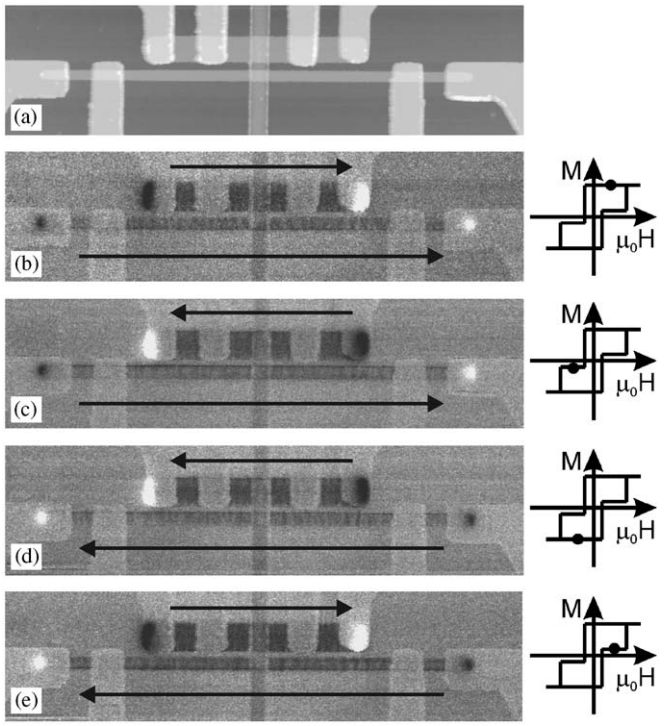

Fig. 3. Stray fields of the permalloy electrodes recorded with a magnetic-force microscope at room temperature. (a) Topography of the device, (b) and (d) show the parallel, (c) and (e) the antiparallel configurations of the magnetizations. The dots in the schematic hysteresis loops indicate the state of the corresponding image. The arrows illustrate the directions of the magnetizations in the electrodes.

4. Magnetotransport measurements

All transport measurements have been performed at liquid-helium temperatures and above using lock-in techniques. The external magnetic field is applied parallel to the long axes of the electrodes.[1] The anisotropic magnetoresistance (AMR) of both electrodes has been recorded to obtain the coercive fields at low temperatures. The exact experimental determination of the AMR is important for the identification of its contribution to the magnetoresistance of the entire device. The AMR of the shorter electrode has been measured by sending an AC current of 5 μA from contact 7 to 9 and probing the voltage at contacts 6 and 8 (see Fig. 1). For the longer electrode the current source has been connected to contacts 2 and 10, and contacts 1 and 11 have been used as voltage probes. Fig. 4(a) and (b) shows the results for the shorter and the longer electrode, respectively. Following the resistance trace for one sweep direction of the external magnetic field, e.g. the up-sweep in Fig. 4(b) indicated by arrows, one observes a reversible negative resistance change when

[1] An offset in magnetic field of −10.0 mT in all measurements is presumably due to the remanence of the superconducting solenoid and was corrected for Figs. 4 and 5.

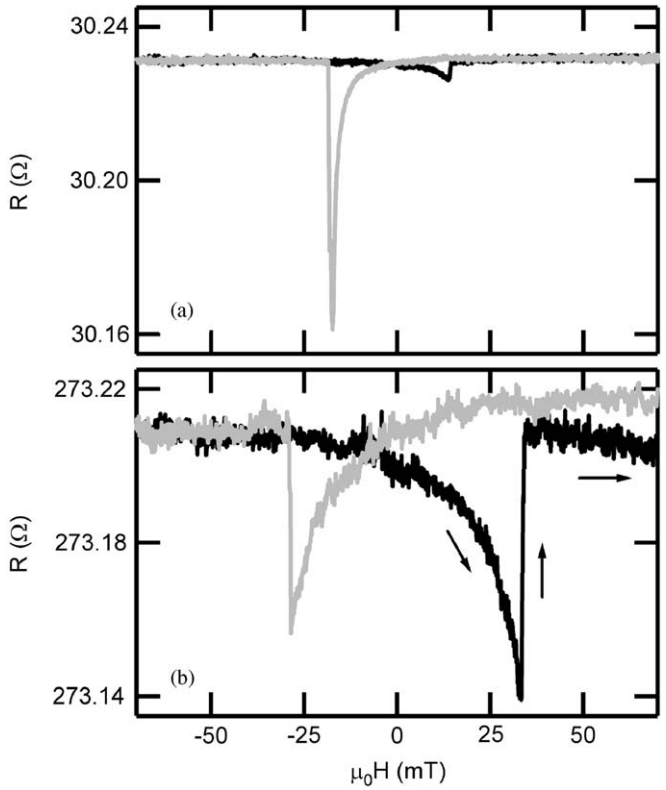

Fig. 4. (a) Anisotropic magnetoresistance of the shorter (a) and the longer electrodes (b). Grey and black lines correspond to the negative and the positive sweep directions of the external magnetic field.

passing zero field. The magnetization reversal process is completed when the resistance rises irreversibly back to its initial value in one sharp flank. The relative resistance changes are 2.3‰ and less. In measurements with the external magnetic field applied perpendicular to the long axes of the electrodes we obtain maximum relative resistance changes of 3.3%. Hence, the magnetization turns only a few degrees away from the easy axes of the electrodes causing the reversible resistance change before the magnetization is fully and irreversibly inverted. This proves the quasi-single-domain behavior already observed at room temperature. At liquid-helium temperatures we measure coercive fields of -18.5 and $+14.5$ mT for the shorter electrode and -29 and $+34$ mT for the longer electrode. While the magnitude of the AMR in both sweep directions is comparable for the longer electrode, for the shorter electrode the effect in the negative sweep direction is an order of magnitude larger than in the positive sweep direction. This is presumably because of the gold contacts which fully overlap the longer electrode while they do not so for the shorter electrode. Therefore, magnetization changes in the shorter electrode on the side directed towards the longer electrode may not be recorded completely in the resistance traces. By assuming that the local magnetization changes of the reversal process differ for both sweep directions, the asymmetrical resistance changes in Fig. 4(a) can be explained.

The magnetoresistance of the F/N/F hybrid device has been recorded by sending a current of 50 μA from contact 1 to 6 and probing the voltage at contacts 11 and 8, i.e. in spin-valve geometry. Fig. 5(a) shows a measurement at a temperature of 2 K. Following, e.g., the positive sweep direction indicated by arrows, one observes a reversible negative resistance change when passing zero field. This is followed by a sharp positive flank rising above the initial value of the resistance in the parallel configuration which cannot be explained by means of AMR. Then the trace shows a plateau which ends in a sharp drop of the resistance. The resistance at positive saturation fields is slightly larger than at negative saturation fields which can be explained by the local Hall effect [13]. Both sharp flanks coincide with the flanks observed in the AMR traces which proves the antiparallel configuration in the plateau region. Therefore, we conclude that this increased resistance is caused by the spin-valve effect. The reversible resistance changes between zero field and the positive flanks in the resistance traces resemble the shape of the AMR measurements of the shorter electrode which leads to the conclusion that this part originates from AMR. The AMR of the longer electrode shows no observable contribution to the overall magnetoresistance. This is reasonably explained by the smaller relative changes of

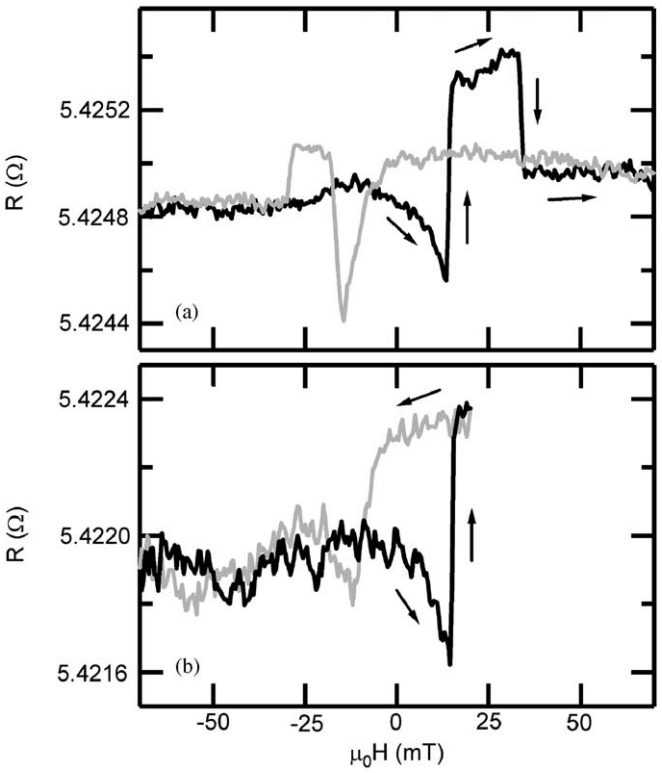

Fig. 5. Magnetoresistance of the entire device recorded in spin-valve geometry at a temperature of 2 K. (a) Shows the full hysteresis, (b) depicts a minor loop beginning in the positive sweep direction. Black and grey lines correspond to the positive and the negative sweep directions of the external magnetic field.

the AMR in comparison to the shorter electrode which shows relative resistance changes an order of magnitude larger (see Fig. 4). To support our interpretations of the different contributions we have recorded minor loops in spin-valve geometry. A result is shown in Fig. 5(b). The turning point of the external magnetic field at +20 mT lies well between the two positive coercive fields of both electrodes (14.5 and 34 mT), thus adjusting an antiparallel configuration at this field strength. Beginning with the positive sweep direction the minor-loop measurement resembles the trace of Fig. 5(a) up to the plateau region. After the turning point to the negative sweep direction, the resistance remains at the plateau niveau up to zero field which is well explained by the spin-valve effect. Then the resistance drops due to the AMR contribution which is followed by an increase back to the resistance level of the parallel configuration at negative fields. The increase at −18.5 mT coincides with the negative coercive field of the shorter electrode (see Fig. 4(a)). Measurements in the non-local geometry, i.e. the current is driven between contacts 5 and 6 and the voltage is probed at contacts 1 and 12, principally produce a pure spin-valve signal without AMR and Hall contributions. However, up to the experimental sensitivity of below 1‰ of our setup, we do not observe the spin-valve effect in the non-local measurements in contrast to Ref. [3].

Using Eq. (3) the absolute resistance change can be compared with the theory. Therefore, we have measured the conductivities of the permalloy and the aluminum in our device to be $\sigma_{Py} = 3.7 \times 10^6\,\Omega^{-1}\,m^{-1}$ and $\sigma_{Al} = 8.6 \times 10^6\,\Omega^{-1}\,m^{-1}$ at liquid-helium temperatures. The device geometry provides the electrode spacing $L = 350$ nm and a cross-sectional area of 600 nm × 25 nm of the aluminum strip. With $I = 50\,\mu A$, $\alpha_F = 0.37$ [14], $\lambda_F = 4.3$ nm [15] and $\lambda_N = 650$ nm [3], we obtain $\Delta\mu = 7.2 \times 10^{-8}$ eV which results in a resistance change ΔR of 1.4 mΩ. The maximum resistance change in our measurements is 0.43 mΩ at a temperature of 2 K in the positive sweep direction. The theoretical description anticipates a simplified geometry of the spin-valve device. However, from diffusive transport simulations we know that the permalloy electrodes are partly shunted by the aluminum strip which could result in an average electrode spacing of 900 nm from the center of one electrode to the center of the other. Using this value as L in Eq. (3) and thus considering the current distribution in the actual geometry of the device leads to a resistance change of 0.45 mΩ which is close to the experimental value.

In Fig. 6(a), the resistance of the entire device is plotted versus the temperature. In Fig. 6(b), the temperature dependence of ΔR is shown for the positive (black triangles) and the negative (grey triangles) sweep direction. For the comparison of the experimental results with the theory we assume that α_F and the ratio of the electron scattering rate τ_{sc}^{-1} and the spin-relaxation rate τ_{sf}^{-1} in both materials are temperature-independent constants [16,17]. Regarding $\sigma \propto \tau_{sc}$ and $\lambda \propto \tau_{sf}$, it is obvious that the ratios σ_F/λ_F and σ_N/λ_N are also temperature independent.

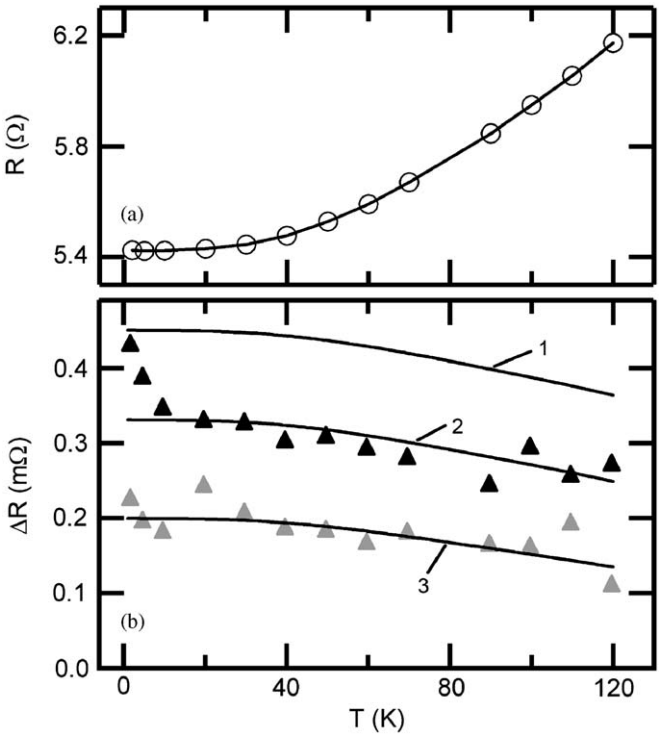

Fig. 6. (a) Circles show the temperature dependence of the resistance of the entire device with the magnetizations of the electrodes aligned parallel. The line is a guide to the eye. (b) Temperature dependence of the resistance changes between parallel and antiparallel configurations of the magnetizations. Grey and black triangles are obtained in negative and positive sweep directions of the external magnetic field. Lines are calculated with Eq. (3) for spin-relaxation lengths at low temperatures of 650 (1), 450 (2) and 320 nm (3).

Accordingly $\cosh(L/\lambda_N)$ and $\sinh(L/\lambda_N)$ are the remaining temperature-dependent factors in Eq. (3). The data in Fig. 6(a) reveal in good approximation the conductivity of the aluminum strip $\sigma_N(T)$. Taking $\sigma_N \propto \lambda_N$ into account leads to the spin-relaxation length

$$\lambda_N(T) = \frac{R(2K)}{R(T)}\lambda_N(2K). \tag{5}$$

We have calculated the temperature dependence of ΔR with the parameters used in this section, especially $L = 900$ nm and $\lambda_N(T)$ as defined in Eq. (5). The results are depicted in Fig. 6(b) for $\lambda_N(2K) = 650$ nm as line 1, $\lambda_N(2K) = 450$ nm as line 2 and $\lambda_N(2K) = 320$ nm as line 3. We conclude that the decrease of the resistance change ΔR with increasing temperature is reasonably explained with the shortening of the spin-relaxation length at higher temperatures. At very low temperatures we observe a tendency of the spin-relaxation length to increase stronger than it can be explained in the theoretical description. We can only speculate that this increase is related to interface effects which have a stronger low-temperature dependence than the decrease of the spin-relaxation length in the bulk that has been considered in the theoretical description.

5. Conclusion

We have identified the AMR, the local Hall effect and the spin-valve effect in a mesoscopic ferromagnet/normal metal device. The experimentally observed resistance changes induced by the spin-valve effect have the same order of magnitude and temperature dependence as expected from the description of the diffusive transport. This supports the interpretation of the observed phenomena as spin-valve effects. In order to enlarge the size of the spin-valve effects, tunnelling barriers are attractive means. Such barriers can be integrated in the device by in situ deposition and oxidation of the aluminum. An alternative path would be the use of electrodes with a higher spin-polarization like Heusler alloys [18].

Acknowledgments

We would like to thank T. Matsuyama and U. Merkt for fruitful discussions and persistent support, J. Gancarz for superb technical assistance, and M. Bolte for the transport simulation. Financial support from the Sonderforschungsbereich 508 "Quantenmaterialien" is gratefully acknowledged.

References

[1] A.T. Hanbicki, B.T. Jonker, G. Itskos, G. Kioseoglou, A. Petrou, Appl. Phys. Lett. 80 (2002) 1240.
[2] H.J. Zhu, M. Ramsteiner, H. Kostial, M. Wassermeier, H.-P. Schönherr, K.H. Ploog, Phys. Rev. Lett. 87 (2001) 016601.
[3] F.J. Jedema, H.B. Heersche, A.T. Filip, J.J.A. Baselmans, B.J. van Wees, Nature 416 (2002) 713.
[4] M.N. Baibich, J.M. Broto, A. Fert, F. Nguyen Van Dau, F. Petroff, P. Eitenne, G. Creuzet, A. Friederich, J. Chazelas, Phys. Rev. Lett. 61 (1988) 2472.
[5] M. Julliere, Phys. Lett. 54A (1975) 225.
[6] J.S. Moodera, L.R. Kinder, T.M. Wong, R. Meservey, Phys. Rev. Lett. 74 (1995) 3273.
[7] Th.G.S.M. Rijks, R. Coehoorn, M.J.M. de Jong, W.J.M. de Jonge, Phys. Rev. B 51 (1995) 283.
[8] Th.G.S.M. Rijks, S.K.J. Lenczowski, R. Coehoorn, W.J.M. de Jonge, Phys. Rev. B 56 (1997) 362.
[9] M. Steiner, C. Pels, G. Meier, J. Appl. Phys. 95 (2004) 6759.
[10] P.C. van Son, H. van Kempen, P. Wyder, Phys. Rev. Lett. 58 (1987) 2271.
[11] A. van Staa, C.M.S. Johnas, U. Merkt, G. Meier, Superlatt. Microstruct. 37 (2005) 349.
[12] T. Last, S. Hacia, M. Wahle, S.F. Fischer, U. Kunze, J. Appl. Phys. 96 (2004) 6706.
[13] F.J. Jedema, M.S. Nijboer, A.T. Filip, B.J. van Wees, Phys. Rev. B 67 (2003) 085319.
[14] R.J. Soulen Jr., J.M. Byers, M.S. Osofsky, B. Nadgorny, T. Ambrose, S.F. Cheng, P.R. Broussard, C.T. Tanaka, J. Nowak, J.S. Moodera, A. Barry, J.M.D. Coey, Science 282 (1998) 85.
[15] S. Dubois, L. Piraux, J.M. George, K. Ounadjela, J.L. Duvail, A. Fert, Phys. Rev. B 60 (1999) 477.
[16] J. Fabian, S. Das Sarma, Phys. Rev. Lett. 83 (1999) 1211.
[17] S. Ingvarsson, L. Ritchie, X.Y. Liu, G. Xiao, J.C. Slonczewski, P.L. Trouilloud, R.H. Koch, Phys. Rev. B 66 (2002) 214416.
[18] S. von Oehsen, J.M. Scholtyssek, C. Pels, G. Neuber, R. Rauer, M. Rübhausen, G. Meier, J. Magn. Magn. Mater. 290–291 (2005) 1371.